Internally Oxidized Ru–Zr Multilayer Coatings

Yung-I Chen *, Tso-Shen Lu and Zhi-Ting Zheng

Institute of Materials Engineering, National Taiwan Ocean University, 2 Pei-Ning Road, Keelung 20224, Taiwan; x76825@gmail.com (T.-S.L.); 10455001@ntou.edu.tw (Z.-T.Z.)

* Correspondence: yichen@mail.ntou.edu.tw; Tel.: +886-2-2462-2192

Abstract: In this study, equiatomic Ru–Zr coatings were deposited on Si wafers at 400 °C by using direct current magnetron cosputtering. The plasma focused on the circular track of the substrate holder and the substrate holder rotated at speeds within 1–30 rpm, resulting in cyclical gradient concentration in the growth direction. The nanoindentation hardness levels of the as-deposited Ru–Zr coatings increased as the stacking periods of the cyclical gradient concentration decreased. After the coatings were annealed in a 1% O_2–99% Ar atmosphere at 600 °C for 30 min, the internally oxidized coatings shifted their respective structures to a laminated structure, misaligned laminated structure, and nanocomposite, depending on their stacking periods. The effects of the stacking period of the cyclical gradient concentration on the mechanical properties and structural evolution of the annealed Ru–Zr coatings were investigated in this study.

Keywords: cyclical gradient concentration; internal oxidation; multilayer coating; nanocomposite coating

1. Introduction

Multilayer nitride coatings with nanoscale layer thickness have exhibited extremely high mechanical hardness due to dislocation blocking by layer interfaces and Hall–Petch strengthening [1]. By contrast, the hardness enhancement in the Y_2O_3/ZrO_2 superlattice has been limited because oxides are brittle materials that are deformed by fracture mechanisms [2]. Two metallic multilayer coatings deposited by cosputtering for immiscible systems, W–Cu [3,4] and Cu–Ta [5,6], have developed a phase-separated nanostructure. However, Ru/Al multilayers have been deposited to fabricate a B2-RuAl intermetallic compound through annealing at approximately 600 °C in a vacuum or Ar [7,8]. Oxide-dispersion-strengthened platinum materials [9] and Ag-oxide-based electric contact material [10] are conventional applications of internal oxidation [11]. Our previous studies [12–15] investigated the internal oxidation of Ru-based alloy multilayer coatings annealed at 600 °C in oxygen-containing atmospheres for the application of protective coatings on glass molding dies. The specific cosputtering processes, which were performed using a substrate holder rotating at a slow speed of one to seven revolutions per minute, have been examined in detail for fabricating Ru–Ta coatings [14]; the fabricated coatings had exposed substrates alternately to the sputter sources without shutter shielding, forming a multilayer structure with a cyclical gradient concentration period at a nanometer scale. An oxidized laminated structure formed because of the inward diffusion of oxygen during the annealing process; this structure comprised alternating oxygen-rich and oxygen-deficient sublayers stacked adjacent to the surface. The inward diffusion of oxygen at 600 °C was dominated by lattice diffusion in the active element-enriched regions [13,16,17]. Because the elements were stacked on the substrate with an alternating gradient concentration, the O atoms could easily diffuse through the paths in the transverse direction, thereby forming oxide sublayers. After the oxygen content in the oxide sublayers reached a saturation level, the grainboundary diffusion along the original columnar structure drove oxygen

to the next period of the laminated structure. During an annealing process conducted at 600 °C in a 1% O_2–99% Ar atmosphere, internal oxidation occurred for Ti–Ru, Zr–Ru, Nb–Ru, Mo–Ru, Hf–Ru, Ta–Ru, and W–Ru coatings, which were prepared using a substrate holder rotating at one revolution per minute [15]; the mechanical properties of the annealed coatings depended on the characteristics of the oxide sublayers. The nanoindentation hardness of the annealed $Zr_{0.30}Ru_{0.70}$ coating exhibited a relatively high value of 18.4 GPa. The widths of the oxide sublayers were restricted by the Ru-dominant sublayers [16,17]; therefore, the internally oxidized coatings can be categorized as nonisostructural oxide/metal multilayers [1]. The substrate holder rotation speed in sputtering affects the stacking period of the laminated structure [14]; therefore, assessing the effect of the stacking period on the mechanical properties of the internally oxidized Ru–Zr coatings is imperative.

2. Materials and Methods

Ru–Zr coatings with a Cr interlayer were fabricated by using magnetron cosputtering onto silicon wafers. Pure metal targets of Ru (99.95%), Zr (99.9%), and Cr (99.95%) with diameters of 50.8 mm each were adopted as source materials for sputtering. The sputter guns were inclined to focus plasma on the circular track of the substrate holder, as described in detail in a previous study [13]. The target-to-substrate distance was maintained at 90 mm for all sputtering runs. The chamber was evacuated down to 2.7×10^{-4} Pa, followed by the inlet of argon gas as a plasma source. The substrate holder was heated to 400 °C and the Ar flow rate was controlled at 20 sccm; the resulting working pressure was 0.7 Pa. The substrate holder was rotated at 1 rpm for depositing the Cr interlayer. Then, Ru–Zr coatings with fixed DC sputtering powers ($W_{Ru} = 100$ W and $W_{Zr} = 200$ W) and various substrate holder rotation speeds were deposited on the Cr interlayer for 25 min. To investigate the internal oxidation phenomenon after performing heat treatments, the Ru–Zr coatings were further annealed at 600 °C in a 1% O_2–99% Ar atmosphere by introducing O_2–Ar mixed gas into a quartz tube furnace.

Chemical composition analysis was conducted by using energy dispersive spectrometry (EDS, Horiba, Kyoto, Japan) equipped with a scanning electron microscope (SEM, S3400N, Hitachi, Tokyo, Japan) on the surface. Surface morphology and thickness evaluation of the coatings were performed by using a field emission scanning electron microscope (FE-SEM, S4800, Hitachi, Tokyo, Japan) at a 15-kV accelerating voltage. A conventional X-ray diffractometer (XRD, X'Pert PRO MPD, PANalytical, Almelo, The Netherlands) with Cu Kα radiation was adopted to identify the phases of the coatings, using the grazing incidence technique with an incidence angle of 1°. The Cu Kα radiation was generated from a Cu anode operated at 45 KV and 40 mA. The nanostructure was examined by using a transmission electron microscope (TEM, JEM-2010F, JEOL, Tokyo, Japan) at a 200-kV accelerating voltage. The TEM samples were prepared by applying a focused ion beam system (FEI Nova 200, Hillsboro, OR, USA) operated at an accelerating voltage of 30 kV with a gallium ion source. A Pt layer was deposited to protect the free surface in the sample preparation. The chemical states of the constituent elements were examined by using an X-ray photoelectron spectroscope (XPS, PHI 1600, PHI, Kanagawa, Japan) with an Mg Kα X-ray beam (energy = 1253.6 eV and power = 250 W) operated at 15 kV. The XPS spectra of O 1s, Ru 3d, and Zr 3d core levels were recorded. Ar+ ion beam of 3 keV was used to sputter the coatings for depth profiling. The surface hardness and Young's modulus of Ru–Zr coatings were measured with a nanoindentation tester (TI-900 Triboindenter, Hysitron, Minneapolis, MN, USA). The nanoindenter was equipped with a Berkovich diamond-probe tip. The applied load was controlled to produce an indentation depth of 80 nm, which is 1/10 of the film thickness [18]. The loading, holding, and unloading times were 5 s each. The nanoindentation hardness and elastic modulus of each indent were calculated using the Oliver and Pharr method [19]. The standard deviations for nanoindentation data were calculated from 8 measurements made at different locations on one sample. The surface roughness values of the coatings, R_a [20], were evaluated by using an atomic force microscope (AFM, Dimension 3100 SPM, NanoScope IIIa, Veeco, Santa Barbara, CA, USA). The scanning area of each image was set at 5×5 μm^2 with a scanning rate of 1.0 Hz.

3. Results

3.1. As-Deposited Equiatomic Ru–Zr Coatings

　　Table 1 lists the chemical compositions of the as-deposited equiatomic Ru–Zr coatings prepared at various substrate holder rotation speeds of 1–30 rpm. The samples were denoted as $Ru_xZr_{1-x}(Ry)$, or Ry, where Ry indicated that the sample prepared using the substrate holder was rotated at y rpm. All the coatings exhibited similar atomic ratios Ru/(Ru + Zr) within 0.46–0.50 after being examined using EDS on the surface, and a thickness of 870–920 nm after being evaluated using FE-SEM in the cross section. Oxygen content in the as-deposited coatings was 0.1–0.5 at.% because of weak oxidation caused by the residual oxygen in the vacuum chamber.

Table 1. Chemical compositions, thickness values, laminated period, mechanical properties, and surface roughness values of $Ru_xZr_{1-x}(Ry)$ coatings as-deposited and annealed at 600 °C in 1% O_2–99% Ar for 30 min.

Sample	Chemical Composition (at.%)			Atomic Ratio	Thickness (nm)		Period (nm)	H (GPa)	E (GPa)	Roughness (nm)
	Ru	Zr	O	Ru:Zr	Coating	Interlayer				
As-deposited										
$Ru_{0.50}Zr_{0.50}$(R1)	50.2	49.6	0.2	50.3:49.7	870	90	34.8	9.1 ± 0.2	128 ± 3	1.76 ± 0.04
$Ru_{0.49}Zr_{0.51}$(R3)	48.7	50.9	0.4	48.9:51.1	900	100	12.0	10.3 ± 0.3	142 ± 3	2.51 ± 0.02
$Ru_{0.48}Zr_{0.52}$(R5)	47.9	51.8	0.3	48.0:52.0	890	100	7.2	10.5 ± 0.6	137 ± 6	3.35 ± 0.06
$Ru_{0.47}Zr_{0.53}$(R10)	47.2	52.3	0.5	47.4:52.6	900	100	3.6	11.0 ± 0.4	161 ± 4	2.62 ± 0.05
$Ru_{0.46}Zr_{0.54}$(R15)	46.3	53.4	0.3	46.4:53.6	900	90	2.4	11.1 ± 0.5	177 ± 7	4.08 ± 0.04
$Ru_{0.47}Zr_{0.53}$(R20)	46.6	53.4	0.1	46.6:53.4	920	95	1.8	11.4 ± 0.6	171 ± 6	1.25 ± 0.01
$Ru_{0.46}Zr_{0.54}$(R30)	46.4	53.6	0.1	46.4:53.6	920	90	1.2	13.1 ± 0.5	172 ± 5	1.37 ± 0.01
Annealed										
$Ru_{0.50}Zr_{0.50}$(R1)	21.3	21.1	57.5	50.1:49.9	1380	110	55.2	15.5 ± 0.4	157 ± 10	5.33 ± 0.50
$Ru_{0.49}Zr_{0.51}$(R3)	21.2	21.2	59.2	48.0:52.0	1370	110	18.1	16.1 ± 0.8	158 ± 8	4.26 ± 0.10
$Ru_{0.48}Zr_{0.52}$(R5)	20.6	20.6	60.7	47.6:52.4	1390	110	11.1	17.2 ± 0.4	178 ± 9	7.02 ± 0.37
$Ru_{0.47}Zr_{0.53}$(R10)	20.3	20.3	61.5	47.3:52.7	1390	110	5.5	12.3 ± 2.1	164 ± 16	17.32 ± 0.53
$Ru_{0.46}Zr_{0.54}$(R15)	20.2	20.2	62.5	46.1:53.9	1390	110	3.7	16.4 ± 1.0	182 ± 6	7.05 ± 0.20
$Ru_{0.47}Zr_{0.53}$(R20)	20.8	20.8	61.3	46.3:53.7	1380	110	2.8	16.1 ± 0.8	160 ± 6	1.89 ± 0.00
$Ru_{0.46}Zr_{0.54}$(R30)	21.0	21.0	61.4	45.7:54.3	1390	110	1.9	17.9 ± 0.7	175 ± 6	5.90 ± 1.05

　　Figure 1 shows cross-sectional SEM images of the as-deposited Ru–Zr coatings, which exhibit a columnar structure. Laminated structures stacked along the growth direction were observed in the $Ru_{0.50}Zr_{0.50}$(R1) and $Ru_{0.49}Zr_{0.51}$(R3) coatings, for which the equilibrated laminated layer periods were 35 and 12 nm, respectively, as determined using the thickness recorded from the SEM observation divided by the number of laminated layers; in other words, the number of revolutions of the substrate holder. Each equilibrated laminated layer period formed as a result of cyclical gradient concentration deposition. The laminated structures of the Ru–Zr(Ry) coatings prepared at higher substrate holder rotation speeds such as $Ru_{0.47}Zr_{0.53}$(R10) and $Ru_{0.46}Zr_{0.54}$(R30) exhibited narrower equilibrated laminated layer periods that could not be evaluated through SEM images.

　　Figure 2 shows the XRD patterns of the as-deposited Ru–Zr(Ry) coatings. The $Ru_{0.50}Zr_{0.50}$(R1), $Ru_{0.49}Zr_{0.51}$(R3), $Ru_{0.48}Zr_{0.52}$(R5), and $Ru_{0.47}Zr_{0.53}$(R10) coatings exhibited reflections of hexagonal Ru [ICDD 06-0663], cubic RuZr [ICDD 18-1147], and hexagonal Zr [ICDD 05-0665] phases, implying that these coatings consisted of laminated sublayers. The equilibrated laminated layer periods for the R5 and R10 coatings were 7.2 and 3.6 nm, respectively. By contrast, XRD patterns of the as-deposited $Ru_{0.46}Zr_{0.54}$(R15), $Ru_{0.47}Zr_{0.53}$(R20), and $Ru_{0.46}Zr_{0.54}$(R30) coatings exhibited a RuZr phase dominant structure. The cubic RuZr phase exhibited XRD reflections of (110), (200), and (211), which are comparable with previous XRD results reported by Mahdouk et al. [21]. RuZr exhibited a B2 structure (CsCl type) [21–25]. Figure 3 depicts a cross-sectional TEM image of the as-deposited $Ru_{0.46}Zr_{0.54}$(R15) coating, which comprises a columnar structure without evident laminated sublayers; the diffraction pattern of the selected area shows a cubic RuZr phase. The equilibrated laminated layer periods for the as-deposited $Ru_{0.46}Zr_{0.54}$(R15), $Ru_{0.47}Zr_{0.53}$(R20), and $Ru_{0.46}Zr_{0.54}$(R30) coatings were 2.4, 1.8, and 1.2 nm, respectively, which were too thin to construct the laminated structure. Under such conditions, the equilibrated laminated layer periods were equal to a variation period of cyclical gradient concentration. Because the substrate temperature was sustained at 400 °C during cosputtering, the

deposited atoms formed an intermetallic RuZr compound, as observed by the XRD patterns. In our previous study [26], B2-RuAl phase was observed for Ru–Al multilayer coatings prepared at 400 °C.
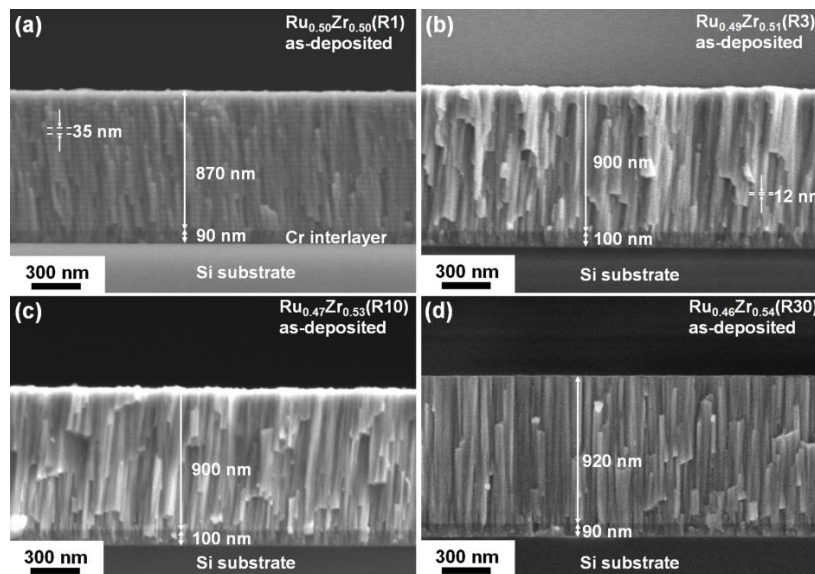

Figure 1. Cross-sectional SEM images of the as-deposited (**a**) $Ru_{0.50}Zr_{0.50}$(R1); (**b**) $Ru_{0.49}Zr_{0.51}$(R3); (**c**) $Ru_{0.47}Zr_{0.53}$(R10); and (**d**) $Ru_{0.46}Zr_{0.54}$(R30) coatings.
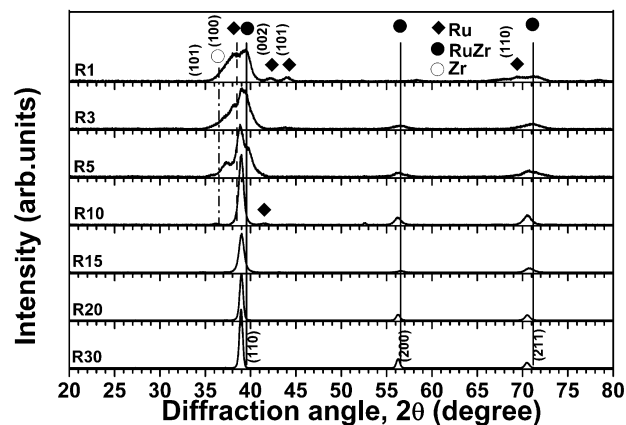
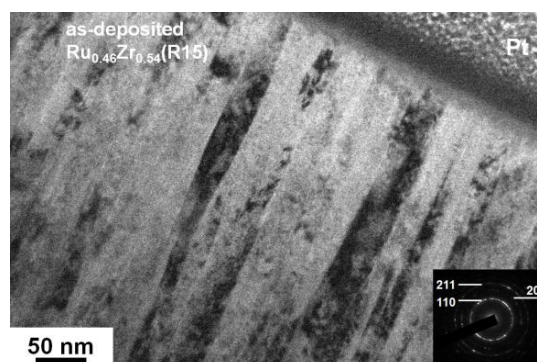**Figure 2.** XRD patterns of the as-deposited Ru–Zr(R*y*) coatings.

Figure 3. Cross-sectional TEM image and selected area diffraction pattern of the as-deposited $Ru_{0.46}Zr_{0.54}$(R15) coating.

3.2. Internally Oxidized Ru–Zr Coatings

Figure 4 shows the cross-sectional SEM image of the annealed $Ru_{0.50}Zr_{0.50}$(R1) coating, which exhibited a laminated structure with an equilibrated laminated layer period of 55 nm. However, the features of the other coatings could not be identified through SEM. Figure 5 presents the XRD patterns of the Ru–Zr coatings after annealing in 1% O_2–99% Ar at 600 °C for 30 min; all patterns exhibited monoclinic ZrO_2 [ICDD 32-1484], tetragonal ZrO_2 [ICDD 42-1164], and Ru phases. The Ru:Zr atomic ratios were maintained at levels similar to those of the as-deposited coatings (Table 1), implying that no volatile oxides were formed during annealing. The O content in the annealed coatings increased to within 58–62 at.%, indicating that extra O was trapped because the stoichiometric ratio of ZrO_2 was two, enabling partial Ru atoms to be oxidized.
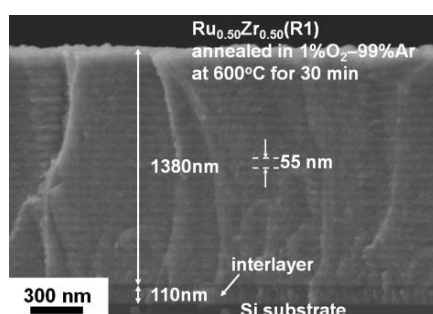

Figure 4. Cross-sectional SEM image of the $Ru_{0.50}Zr_{0.50}$(R1) coating after annealing in 1% O_2–99% Ar at 600 °C for 30 min.
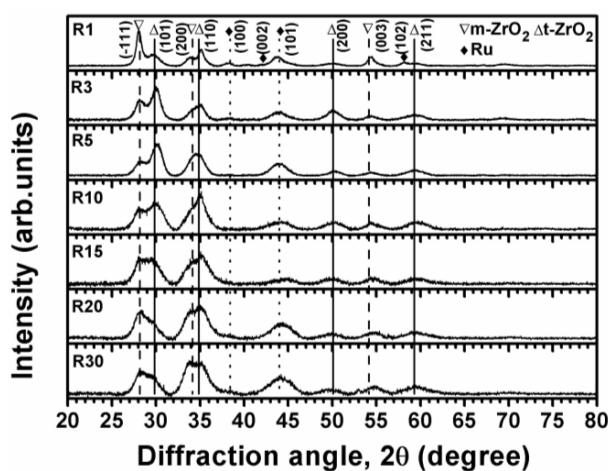

Figure 5. XRD patterns of the Ru–Zr(R*y*) coatings after annealing in 1% O_2–99% Ar at 600 °C for 30 min.

Figure 6a–c illustrates the XPS spectra of O 1s, Zr 3d, and Ru 3d core levels, respectively, at various thickness levels of the annealed $Ru_{0.50}Zr_{0.50}$(R1) coating. The detected depth crossed six periods of the laminated layers. The O and Zr species were identified as O^{2-} and Zr^{4+}, whereas Ru was identified as Ru^0 except for the spectra near the surface region (depth < 13 nm), where the Ru^{x+} and Ru^{4+} signals were split. The binding energy value of Ru^0 $3d_{5/2}$ (279.96 ± 0.08 eV) was consistent with that of other coatings (279.69–280.16 eV) reported in the literature [13,16,17,27], whereas the binding energies of Ru^{x+} and Ru^{4+} $3d_{5/2}$ were 280.45 ± 0.11 and 282.57 ± 0.15 eV, respectively. Previous studies reported 281.4–282.2 eV [26,28–30] for the binding energy of Ru^{4+} $3d_{5/2}$. Ru of 17%–20% exhibited the Ru^{4+} state at a depth of 0–13 nm. Ru atoms remained in its metallic state beneath the near surface region. Figure 6d shows the intensity variations of O^{2-} 1s, Ru^0 $3d_{5/2}$, and Zr^{4+} $3d_{5/2}$ signals along the depth, which indicates that the variation trend of the

O^{2-} 1s profile coincides with that of the Zr^{4+} $3d_{5/2}$ profile and is in contrast to that of the Ru^0 $3d_{5/2}$ profile, implying that ZrO_2 is the dominant oxide. Therefore, the annealed $Ru_{0.50}Zr_{0.50}(R1)$ coating comprised alternating oxygen-rich and oxygen-deficient layers stacked along the O-diffusion direction. The binding energy value of Zr^{4+} $3d_{5/2}$ deviated within 182.05–183.35 eV (Figure 6e). Moreover, this range decreased to 182.71–183.35 eV after the data in the first laminated period had been excluded. Previous studies have reported 182.75 [31], 182.8 [32], and 182.9 eV [33] for the binding energy value of Zr^{4+} $3d_{5/2}$. The binding energy value of O^{2-} 1s demonstrated a variation pattern similar to that of the binding energy value of Zr^{4+} $3d_{5/2}$ (Figure 6e). The charging effect of analyzing insulators [34] caused substantial deviation in binding energy. The binding energy difference $\Delta = (O^{2-}$ 1s $- Zr^{4+}$ $3d_{5/2})$ was 347.92 ± 0.05 eV at the analyzed depth of 19.5–318.5 nm. This difference was highly consistent with the reported difference of 348.01 and 348.2 eV, calculated using 530.76 and 182.75 eV [31] or 531.1 and 182.9 eV [33] for O^{2-} 1s and Zr^{4+} $3d_{5/2}$, respectively. The periodic changes of nonoxidized metallic Ru suggested the influence of oxygen in the Zr-deficient sublayers.
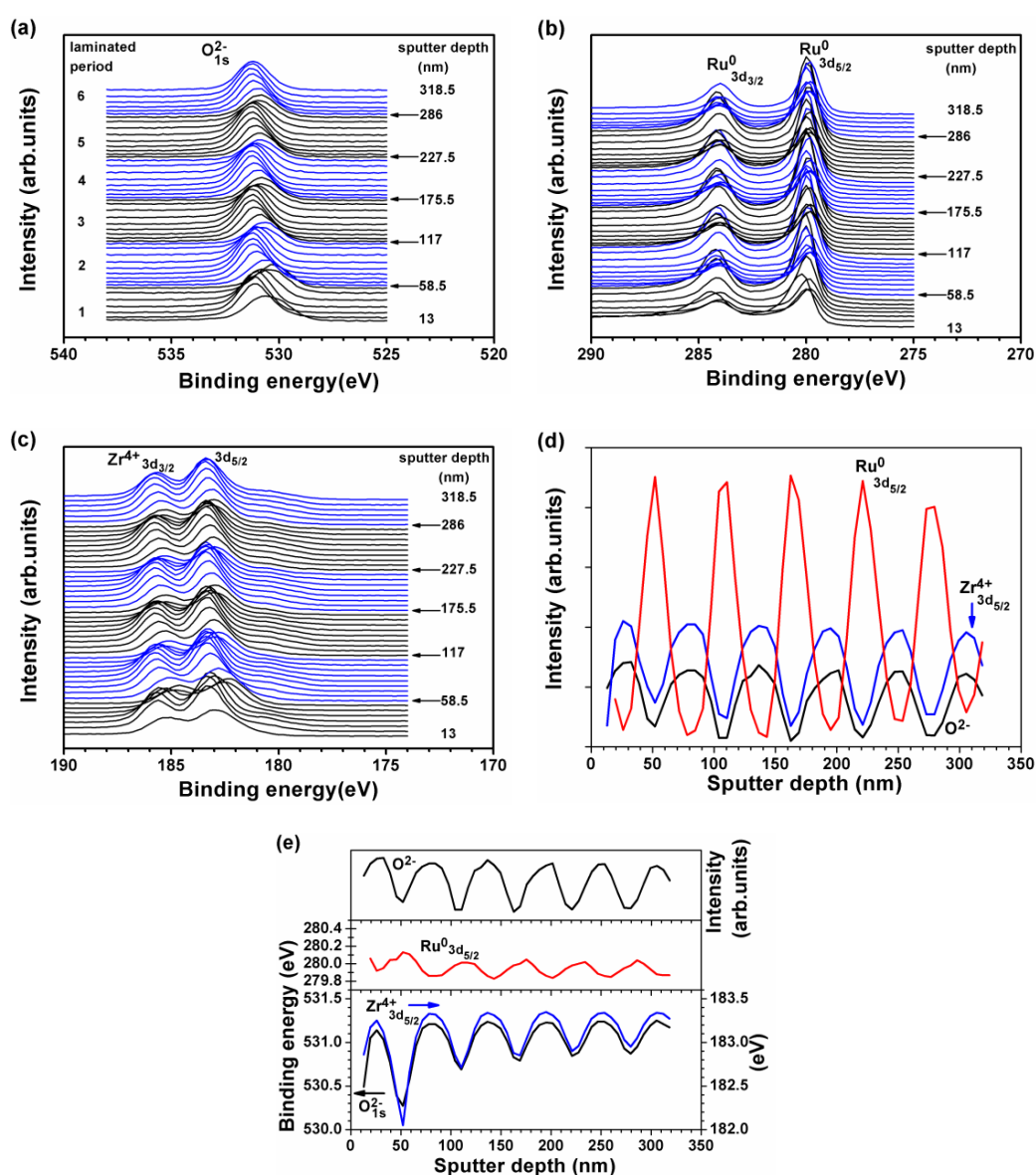

Figure 6. XPS spectra of (**a**) O 1s, (**b**) Ru 3d, and (**c**) Zr 3d core levels of the $Ru_{0.50}Zr_{0.50}(R1)$ coating after annealing in 1% O_2–99% Ar at 600 °C for 30 min; variation patterns of (**d**) intensity and (**e**) binding energy of O^{2-}1s, $Zr^{4+}3d_{5/2}$, and Ru^0 $3d_{5/2}$.

Figure 7a,b shows the cross-sectional TEM images of the annealed $Ru_{0.48}Zr_{0.52}$(R5) coating; the laminated structure was evident. Figure 7c shows a high-resolution TEM image of the near-surface region of the annealed coating. The lattice fringes of particular areas indicated that the annealed $Ru_{0.48}Zr_{0.52}$(R5) coating comprised ZrO_2- and Ru-dominant sublayers, which linked together across the original columnar boundaries such that the annealed $Ru_{0.48}Zr_{0.52}$(R5) coatings were laminated and the columnar boundaries were unresolved. Figure 8a depicts the cross-sectional TEM image of the annealed $Ru_{0.47}Zr_{0.53}$(R10) coating. The laminated sublayers were curved, because of which the stacks of sublayers among neighboring columnar structures were disconnected. Figure 8b shows the high-resolution TEM image of the middle region of the annealed $Ru_{0.47}Zr_{0.53}$(R10) coating. The Ru-dominant sublayers were two-nanometers thick only, and disconnected regions of the sublayers among neighboring columnar structures were observed. The fast variation of cyclical gradient concentration for the R10 coatings prepared with a quick substrate holder rotation speed resulted in the formation of grooved sublayers. For the coatings with thicker Ru sublayers, R1, R3, and R5, the sublayers became flat. The misaligned connections were more evident in the near-surface region (Figure 8c).
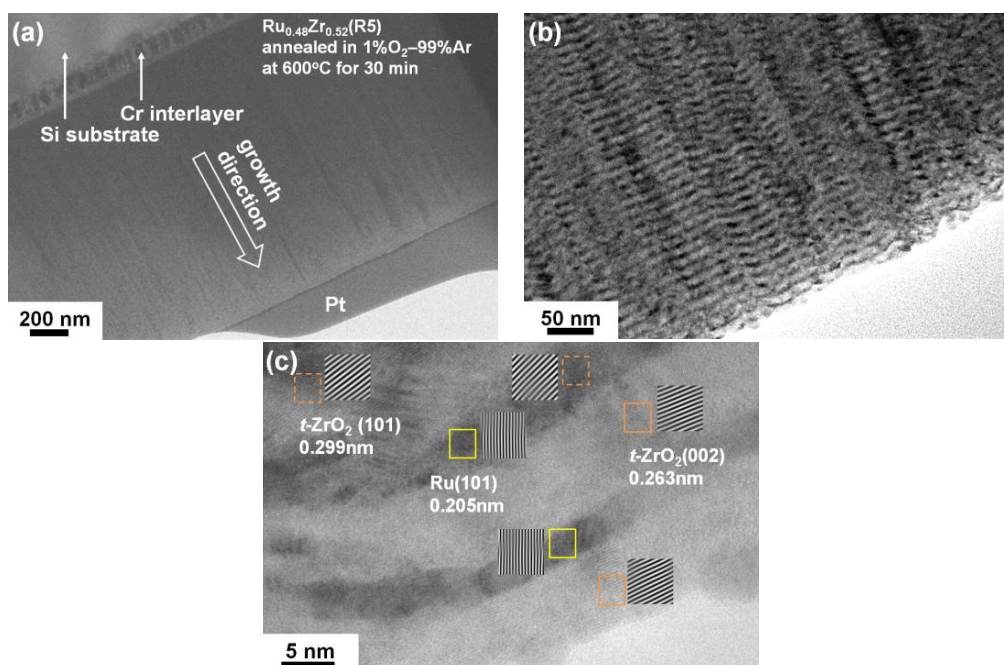

Figure 7. (**a**,**b**) cross-sectional TEM images of the oxidized $Ru_{0.48}Zr_{0.52}$(R5) coating; (**c**) high-resolution image of the near surface region of the annealed $Ru_{0.48}Zr_{0.52}$(R5) coating.
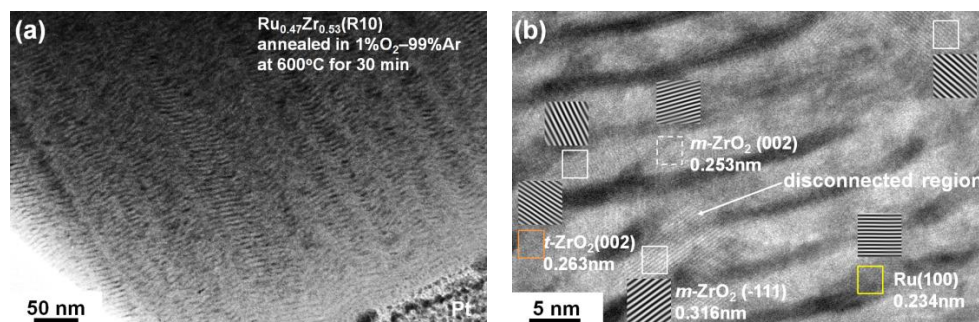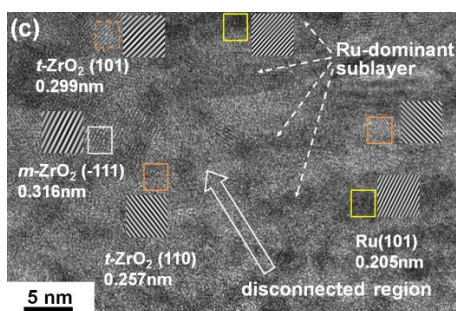

Figure 8. *Cont.*

Figure 8. (**a**) Cross-sectional TEM image of the oxidized $Ru_{0.47}Zr_{0.53}$(R10) coating; high-resolution images of the (**b**) middle region and (**c**) near-surface region of the annealed coating.

Figure 9a shows a cross-sectional TEM image of the annealed $Ru_{0.46}Zr_{0.54}$(R30) coating, in which the original columnar boundaries are evident, but no laminated structures were observed. A high-resolution TEM image (Figure 9b) revealed nanocrystalline grains of ZrO_2 and Ru, each approximately five nanometers in diameter, implying that a nanocomposite structure had been constructed. Furthermore, Ru grains, the dark regions in the image, tended to concentrate along the columnar boundaries. Figure 10a–c illustrates the XPS spectra of the annealed $Ru_{0.46}Zr_{0.54}$(R30) coating. The XPS spectra of Ru 3d core levels indicated the presence of minor Ru^{4+} ($3d_{5/2}$: 282.11 eV) in addition to Ru^0 ($3d_{5/2}$: 280.19 $\pm$ 0.07 eV) at the near-surface region (Figure 10b), which was attributed to the incorporation of Ru into the ZrO_2 grains because RuO_2 and ZrO_2 possessed a similar tetragonal structure. Figure 10d shows that the intensities of O^{2-} 1s, Ru^0 $3d_{5/2}$, and Zr^{4+} $3d_{5/2}$ signals were constant along the depth due to the limit of XPS analyses. Similar binding energy trends were observed for O^{2-} and Zr^{4+} (Figure 10e). The binding energy difference $\Delta = (O^{2-}$ 1s $- Zr^{4+}$ $3d_{5/2})$ was 348.00 ± 0.02 eV at the analyzed depth (5.7–96.9 nm). Therefore, Zr reacted with O during annealing, and the annealed coating exhibited a nanocomposite comprising ZrO_2 and Ru grains.
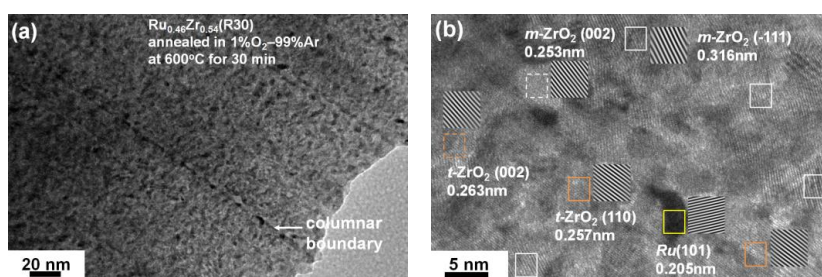

Figure 9. (**a**) Cross-sectional TEM image and (**b**) high-resolution image of the oxidized $Ru_{0.46}Zr_{0.54}$(R30) coating.
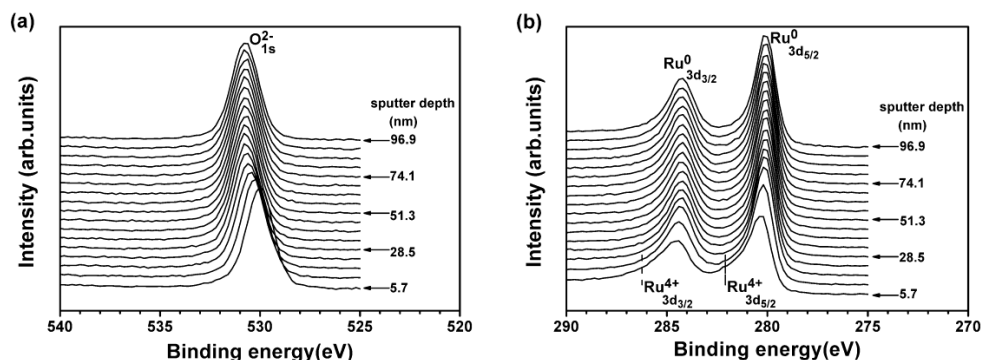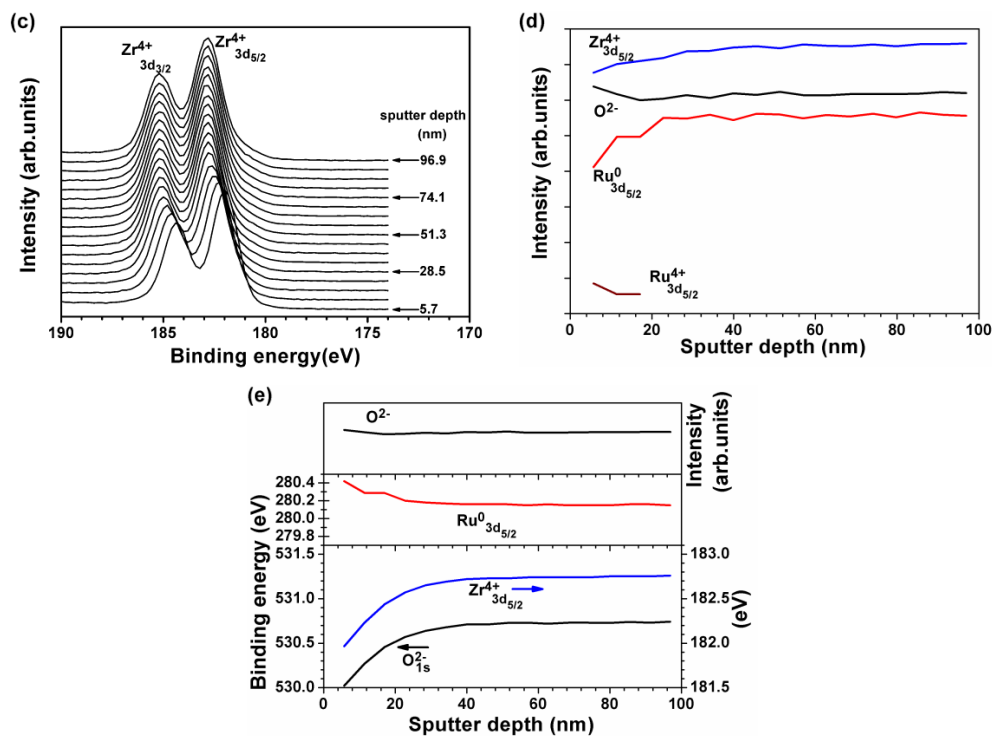

Figure 10. *Cont.*

Figure 10. XPS spectra of (**a**) O 1s, (**b**) Ru 3d, and (**c**) Zr 3d core levels of the $Ru_{0.46}Zr_{0.54}$(R30) coating after annealing in 1% O_2–99% Ar at 600 °C for 30 min; variation patterns of (**d**) intensity and (**e**) binding energy of O^{2-}1s, $Zr^{4+}3d_{5/2}$, and Ru^0 $3d_{5/2}$.

3.3. Mechanical Properties of Internally Oxidized Ru–Zr Coatings

Figure 11 depicts the nanoindentation hardness variations of the as-deposited and internally oxidized Ru–Zr coatings prepared at various substrate holder rotation speeds through sputtering. The hardness of the as-deposited coatings increased from 9.1 to 13.1 GPa with the substrate holder rotation speed and decreasing equilibrated laminated layer period. This hardness increase was attributed to the decrease in crystalline size and structural variation. The nanoindentation hardness of all Ru–Zr coatings increased after annealing in 1% O_2–99% Ar at 600 °C for 30 min. The hardness variation curve of the internally oxidized Ru–Zr coatings exhibited three divisions representing a laminated structure, a disconnected laminated structure, and a nanocomposite region. The hardness increased from 9.1, 10.3, and 10.5 to 15.5, 16.1, and 17.2 GPa for the annealed $Ru_{0.50}Zr_{0.50}$(R1), $Ru_{0.49}Zr_{0.51}$(R3), and $Ru_{0.48}Zr_{0.52}$(R5) coatings, respectively, which exhibited equilibrated laminated layer periods of 55, 18, and 11 nm, respectively. This result indicates that the hardness of the internally oxidized Ru–Zr coatings, which exhibited crystalline phases identical to those identified through XRD analysis and appropriately maintained their multilayer structures, was affected by the layer period. These internally oxidized Ru–Zr multilayer coatings were categorized as nonisostructural oxide/metal multilayers [1]. Dislocation could not be moved across oxide/metal interfaces because oxides are brittle materials that deform through fracture mechanisms, limiting the hardness enhancement [2]; therefore, the hardness of oxide/metal multilayers approached that of the oxide ZrO_2. Gan et al. reported a nanoindentation hardness of 18 GPa for monoclinic ZrO_2 thin films [35]. By contrast, the hardness of the annealed $Ru_{0.47}Zr_{0.53}$(R10) coatings with an equilibrated laminated layer period of 5.6 nm exhibited a relatively low level of 12.3 GPa. Although the internally oxidized $Ru_{0.47}Zr_{0.53}$(R10) coatings were laminated in each columnar structure, the same sublayers among neighboring columnar structures were misaligned and disconnected, which reduced the hardness. The internally oxidized $Ru_{0.46}Zr_{0.54}$(R15), $Ru_{0.47}Zr_{0.53}$(R20), and $Ru_{0.46}Zr_{0.54}$(R30) coatings exhibited high hardness within 16.1–17.9 GPa and were categorized as nanocrystalline composites consisting of hard ZrO_2 grains and

soft Ru grains. Figure 12 shows the variation in Young's moduli of the as-deposited and internally oxidized Ru–Zr coatings. The Young's moduli increased from 130 to 140 GPa for R1, R3, and R5 coatings, to 160 GPa for R10 coatings and 170–180 GPa for R15, R20, and R30 coatings. Because the internally oxidized Ru–Zr coatings exhibited similar phases, ZrO_2 and Ru, the differences in Young's moduli among the annealed coatings were limited (i.e., 160–180 GPa). The surface roughness values of the Ru–Zr coatings are shown in Table 1. When evaluating the mechanical properties of coatings, previous studies [36–38] have reported that coatings with higher surface roughness exhibit larger standard deviation values or lower mean values. The effect of surface roughness on the mechanical properties of as-deposited Ru–Zr coatings was unclear. By contrast, the mechanical properties of the annealed coatings revealed larger deviations and higher surface roughness values than did those of the as-deposited coatings.
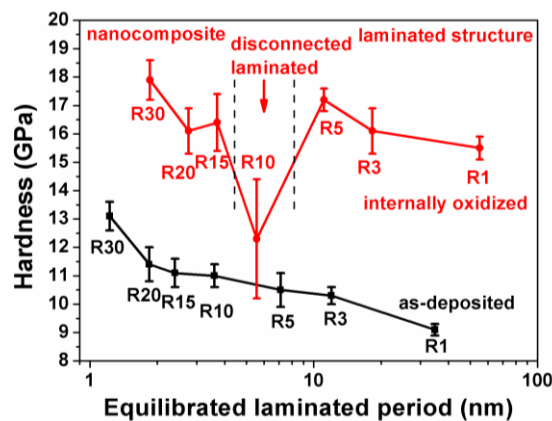

Figure 11. Nanoindentation hardness values of the as-deposited and internally oxidized Ru–Zr coatings.
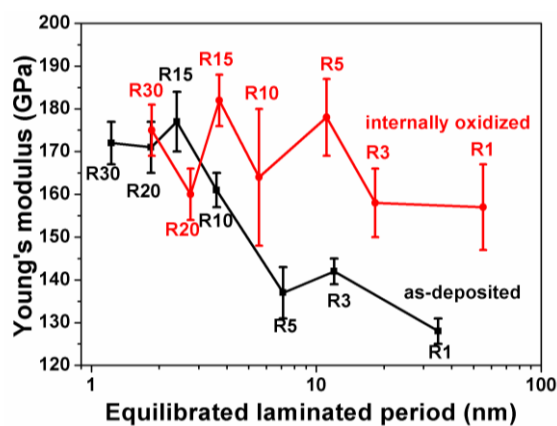

Figure 12. Young's modulus values of the as-deposited and internally oxidized Ru–Zr coatings.

4. Conclusions

Rotation speeds of the substrate holder during sputtering affected the crystalline structure and mechanical properties of Ru–Zr coatings both in the as-deposited and internally oxidized states. Because Ru–Zr coatings were fabricated using a cyclical gradient concentration stacked constitution, the coatings prepared at low rotation speeds (1–10 rpm) exhibited a laminated structure in addition to a columnar structure. The as-deposited Ru–Zr coatings exhibited nanoindentation hardness of 9.1–13.1 GPa, and the coatings prepared at higher substrate holder rotation speeds exhibited higher hardness. After annealing in a 1% O_2–99% Ar atmosphere at 600 °C for 30 min accompanied by the conduction of internal oxidation, the coatings prepared at a substrate holder rotation speed of one to five revolutions

per minute maintained a laminated structure; this structure comprised alternately stacked Ru-dominant and ZrO_2-dominant sublayers whose nanoindentation hardness increased to 15.5–17.2 GPa because of the formation of ZrO_2 phase and the maintenance of sublayer interfaces. By contrast, the annealed coatings prepared at a rotation speed of 10 rpm maintained a similar laminated structure; however, the stacks of sublayers among neighboring columnar structures were misaligned and disconnected, resulting in relatively low nanoindentation hardness of 12.3 GPa. The annealed coatings prepared at a substrate holder rotation speed of 15–30 rpm exhibited nanocomposite coatings comprising Ru and ZrO_2 grains within evident columnar boundaries and a high nanoindentation hardness of 16.1–17.9 GPa.

Author Contributions: Yung-I Chen designed the experiments and wrote the paper; Tso-Shen Lu performed the experiments; Zhi-Ting Zheng analyzed the XPS data.

Conflicts of Interest: The authors declare no conflict of interest. The founding sponsors had no role in the design of the study; in the collection, analyses, or interpretation of data; in the writing of the manuscript, and in the decision to publish the results.

References

1. Yashar, P.C.; Sproul, W.D. Nanometer scale multilayered hard coatings. *Vacuum* **1999**, *55*, 179–190. [CrossRef]
2. Yashar, P.C.; Barnett, S.A.; Hultman, L.; Sproul, W.D. Deposition and mechanical properties of polycrystalline Y_2O_3/ZrO_2 superlattices. *J. Mater. Res.* **1999**, *14*, 3614–3622. [CrossRef]
3. Vüllers, F.T.N.; Spolenak, R. From solid solutions to fully phase separated interpenetrating networks in sputter deposited "immiscible" W–Cu thin films. *Acta Mater.* **2015**, *99*, 213–227. [CrossRef]
4. Beainou, R.E.; Martin, N.; Potin, V.; Pedrosa, P.; Yazdi, M.A.P.; Billard, A. Correlation between structure and electrical resistivity of W–Cu thin films prepared by GLAD co-sputtering. *Surf. Coat. Technol.* **2017**, *313*, 1–7. [CrossRef]
5. Müller, C.M.; Sologubenko, A.S.; Gerstl, S.S.A.; Süess, M.J.; Courty, D.; Spolenak, R. Nanoscale Cu/Ta multilayer deposition by co-sputtering on a rotating substrate. Empirical model and experiment. *Surf. Coat. Technol.* **2016**, *302*, 284–292. [CrossRef]
6. Müller, C.M.; Spolenak, R. An in situ X-ray diffraction study of phase separation in Cu–Ta alloy thin films. *Thin Solid Films* **2016**, *598*, 276–288. [CrossRef]
7. Zotov, N.; Woll, K.; Mücklich, F. Phase formation of B2-RuAl during annealing of Ru/Al multilayers. *Intermetallics* **2010**, *18*, 1507–1516. [CrossRef]
8. Guitar, M.A.; Aboulfadl, H.; Pauly, C.; Leibenguth, P.; Migot, S.; Mücklich, F. Production of single-phase intermetallic films from Ru-Al multilayers. *Surf. Coat. Technol.* **2014**, *244*, 210–216. [CrossRef]
9. Manhardt, H.; Lupton, D.F.; Kock, W. Gold-Free Platinum Material Dispersion-Strengthened by Small, Finely Dispersed Particles of Base Metal Oxide. U.S. Patent 6,663,728, 16 December 2003.
10. Nakamura, T.; Sakaguchi, O.; Kusamori, H.; Matsuzawa, O.; Takahashi, M.; Yamamoto, T. Method for Preparing Ag-ZnO Electric Contact Material and Electric Contact Material Produced Thereby. U.S. Patent 6,432,157, 13 August 2002.
11. Khanna, A.S. *Introduction to High Temperature Oxidation and Corrosion*; ASM International: Materials Park, OH, USA, 2002.
12. Chen, Y.I.; Chang, L.C.; Huang, R.T.; Tsai, B.N.; Kuo, Y.C. Internal Oxidation of Mo–Ru Coatings. *Thin Solid Films* **2010**, *518*, 3819–3824. [CrossRef]
13. Chen, Y.I.; Tsai, B.N. Annealing and oxidation study of Ta–Ru hard coatings. *Surf. Coat. Technol.* **2010**, *205*, 1362–1367. [CrossRef]
14. Chen, Y.I. Laminated structure in internally oxidized Ru–Ta coatings. *Thin Solid Films* **2012**, *524*, 205–210. [CrossRef]
15. Chen, Y.I.; Chu, H.N.; Chang, L.C.; Lee, J.W. Internal oxidation and mechanical properties of Ru based alloy coatings. *J. Vac. Sci. Technol. A* **2014**, *32*, 02B101. [CrossRef]

16. Chen, Y.I.; Lu, T.S. Internal oxidation of laminated ternary Ru–Ta–Zr coatings. *Appl. Surf. Sci.* **2015**, *353*, 245–253. [CrossRef]

17. Chen, Y.I.; Chu, H.N.; Kai, W. Internal oxidation of laminated Nb–Ru coatings. *Appl. Surf. Sci.* **2016**, *389*, 477–483. [CrossRef]

18. Saha, R.; Nix, W.D. Effects of the substrate on the determination of thin film mechanical properties by nanoindentation. *Acta Mater.* **2002**, *50*, 23–38. [CrossRef]

19. Oliver, W.C.; Pharr, G.M. An improved technique for determining hardness and elastic modulus using load and displacement sensing indentation experiments. *J. Mater. Res.* **1992**, *7*, 1564–1583. [CrossRef]

20. Bennett, J.M. *Rough Surfaces*, 2nd ed.; Imperial College Press: London, UK, 1999.

21. Mahdouk, K.; Elaissaoui, K.; Charles, J.; Bouirden, L.; Gachon, J.C. Calorimetric study and optimization of the ruthenium-zirconium phase diagram. *Intermetallics* **1997**, *5*, 111–116. [CrossRef]

22. Wang, F.E. Equiatomic binary compounds of Zr with transition elements Ru, Rh, and Pd. *J. Appl. Phys.* **1967**, *38*, 822–824. [CrossRef]

23. David, N.; Benlaharche, T.; Fiorani, J.M.; Vilasi, M. Thermodynamic modeling of Ru–Zr and Hf–Ru systems. *Intermetallics* **2007**, *15*, 1632–1637. [CrossRef]

24. Arikan, N.; Bayhan, Ü. *Ab initio* calculation of structural, electronic and phonon properties of ZrRu and ZrZn in B2 phase. *Phys. B* **2011**, *406*, 3234–3237. [CrossRef]

25. Xing, W.; Chen, X.Q.; Li, D.; Li, Y.; Fu, C.L.; Meschel, S.V.; Ding, X. First-principles studies of structural stabilities and enthalpies of formation of refractory intermetallics: TM and TM3 (T = Ti, Zr, Hf; M = Ru, Rh, Pd, Os, Ir, Pt). *Intermetallics* **2012**, *28*, 16–24. [CrossRef]

26. Chen, Y.I.; Zheng, Z.T.; Kai, W.; Huang, Y.R. Oxidation behavior of Ru–Al multilayer coatings. *Appl. Surf. Sci.* **2017**, *406*, 1–7. [CrossRef]

27. Chen, Y.I.; Chang, L.C.; Lee, J.W.; Lin, C.H. Annealing and oxidation study of Mo–Ru hard coatings on tungsten carbide. *Thin Solid Films* **2009**, *518*, 194–200. [CrossRef]

28. Rochefort, D.; Dabo, P.; Guay, D.; Sherwood, P.M.A. XPS investigations of thermally prepared RuO_2 electrodes in reductive conditions. *Electrochim. Acta* **2003**, *48*, 4245–4252. [CrossRef]

29. Chen, Y.I.; Chen, S.M.; Chang, L.C.; Chu, H.N. X-ray photoelectron spectroscopy and transmission electron microscopy study of internally oxidized Nb–Ru coatings. *Thin Solid Films* **2013**, *544*, 491–495. [CrossRef]

30. Cox, P.A.; Goodenough, J.B.; Tavener, P.J.; Telles, D.; Egdell, R.G. The electronic structure of $Bi_{2-x}Gd_xRu_2O_7$ and RuO_2: A study by electron spectroscopy. *J. Solid State Chem.* **1986**, *62*, 360–370. [CrossRef]

31. Morant, C.; Sanz, J.M.; Galán, L.; Soriano, L.; Rueda, F. An XPS study of the interaction of oxygen with zirconium. *Surf. Sci.* **1989**, *218*, 331–345. [CrossRef]

32. Maurice, V.; Salmeron, M.; Somorjai, G.A. The epitaxial growth of zirconium oxide thin films on Pt (111) single crystal surfaces. *Surf. Sci.* **1990**, *237*, 116–126. [CrossRef]

33. Wang, Y.M.; Li, Y.S.; Wong, P.C.; Mitchell, K.A.R. XPS studies of the stability and reactivity of thin films of oxidized zirconium. *Appl. Surf. Sci.* **1993**, *72*, 237–244. [CrossRef]

34. Ramana, C.V.; Atuchin, V.V.; Kesler, V.G.; Kochubey, V.A.; Pokrovsky, L.D.; Shutthanandan, V.; Becker, U.; Ewing, R.C. Growth and surface characterization of sputter-deposited molybdenum oxide thin films. *Appl. Surf. Sci.* **2007**, *253*, 5368–5374. [CrossRef]

35. Gan, Z.; Yu, G.; Zhao, Z.; Tan, C.M.; Tay, B.K. Mechanical properties of zirconia thin films deposited by filtered cathodic vacuum arc. *J. Am. Ceram. Soc.* **2005**, *88*, 2227–2229. [CrossRef]

36. Qasmi, M.; Delobelle, P. Influence of the average roughness R_{ms} on the precision of the Young's modulus and hardness determination using nanoindentation technique with a Berkovich indenter. *Surf. Coat. Technol.* **2007**, *201*, 1191–1199. [CrossRef]

37. Walter, C.; Antretter, T.; Daniel, R.; Mitterer, C. Finite element simulation of the effect of substrate roughness on nanoindentation of thin films with spherical indenters. *Surf. Coat. Technol.* **2007**, *202*, 1103–1107. [CrossRef]

38. Kim, J.Y.; Kang, S.K.; Lee, J.J.; Jang, J.; Lee, Y.H.; Kwon, D. Influence of surface-roughness on indentation size effect. *Acta Mater.* **2007**, *55*, 3555–3562. [CrossRef]